Automated Temporal Tracking of Coherently Evolving Density Fronts in Numerical Models

XIAODONG WU,[a] FALK FEDDERSEN,[a] AND SARAH N. GIDDINGS[a]

[a] *Scripps Institution of Oceanography, La Jolla, California*

(Manuscript received 27 May 2021, in final form 8 October 2021)

ABSTRACT: Oceanic density fronts can evolve, be advected, or propagate as gravity currents. Frontal evolution studies require methods to temporally track evolving density fronts. We present an automated method to temporally track these fronts from numerical model solutions. First, at all time steps contiguous density fronts are detected using an edge detection algorithm. A front event, defined as a set of sequential-in-time fronts representing a single time-evolving front, is then identified. At time step i, a front is compared to each front at time step $i + 1$ to determine if the two fronts are matched. An i front grid point is trackable if the minimum distance to the $i + 1$ front falls within a range. The i front is forward matched to the $i + 1$ front when a sufficient number of grid points are trackable and the front moves onshore. A front event is obtained by forward tracking a front for multiple time steps. Within an event, the times that a grid point can be tracked is its connectivity and a pruning algorithm using a connectivity cutoff is applied to extract only the coherently evolving components. This tracking method is applied to a realistic 3-month San Diego Bight model solution yielding 81 front events with duration ≥ 7 h, allowing analyses of front event properties including occurrence frequency and propagation velocity. Sensitivity tests for the method's parameters support that this method can be straightforwardly adapted to track evolving fronts of many types in other regions from both models and observations.

KEYWORDS: Fronts; Algorithms; Numerical analysis/modeling; Ocean models

1. Introduction

Oceanic density fronts are narrow zones of intense physical and biological activity (e.g., Acha et al. 2004; Belkin 2021), which can enhance vertical mixing (D'Asaro et al. 2011) and affect the transport of biogeochemical tracers (e.g., Nagai et al. 2015; Lévy et al. 2018). Density fronts are ubiquitous on continental shelves as identified from in situ observations (e.g., Farrar et al. 2007; Connolly and Kirincich 2019; Spydell et al. 2021), detected in radar sensed surface roughness images (e.g., Celona et al. 2021), satellite sea surface temperature (SST) images (e.g., Kahru et al. 2012), and from coastal numerical models (e.g., Dauhajre et al. 2017; Wu et al. 2021b). Dye and SST measurements showed frontal variability within 1 km from shore (Hally-Rosendahl et al. 2015; Grimes et al. 2020). Fronts alter Lagrangian transport pathways (Banas et al. 2009) and affect the distribution of larval species (Pineda 1999) over the shelf. Many processes are responsible for front generation, including wind-driven upwelling (Austin and Lentz 2002), freshwater discharge (Horner-Devine et al. 2015) and propagation of nonlinear internal waves (NLIWs) (e.g., Suanda et al. 2014; Badiey et al. 2016; Colosi et al. 2018; McSweeney et al. 2020a). Upon generation, a density front is characterized by its kinematics (e.g., length, direction, and intensity) and behavior (e.g., displacement and deformation). Capturing and tracking frontal displacement potentially allows a Lagrangian approach to examine frontal dynamics.

Tracking frontal displacement first requires front detection. Given the rapidly growing dataset from remote sensing (SST and surface roughness) and numerical models, a variety of automatic front detection approaches have been proposed, and a comprehensive review of these approaches is provided in Hopkins et al. (2010) and Belkin (2021). Among them, two widely used approaches are the Cayula–Cornillon method that uses histogram-based separation of two water masses (Cayula and Cornillon 1992), and gradient-based edge detection, including the Canny method (Canny 1986) that computes horizontal gradients using convolution operators. The Cayula–Cornillon method has been applied to detect satellite SST/chlorophyll fronts (e.g., Ullman and Cornillon 2000; Kahru et al. 2012, 2018). Edge detection has been used to detect satellite SST fronts (e.g., Castelao et al. 2006; Oram et al. 2008) and internal wave fronts from satellite synthetic aperture radar data (e.g., Kurekin et al. 2020). In addition to remote sensing studies, the Cayula–Cornillon method (e.g., Chakraborty et al. 2019) and edge detection (e.g., Mauzole et al. 2020; Wu et al. 2021b) have been used to detect fronts in ocean/shelf numerical models. Wu et al. (2021b) applied the Canny method and detected surface density fronts in a high-resolution, realistic coastal numerical model during a 3-month study period, allowing a statistical analysis of frontal kinematics and an ensemble analysis of frontal dynamics.

In addition to kinematics, density fronts also exhibit behaviors. A front can be advected by background currents (e.g., Austin and Barth 2002; Giddings et al. 2012) or propagate as a gravity current (e.g., Lentz et al. 2003). In the coastal ocean, NLIWs can be generated and propagate onshore in the form of internal wave bores and internal solitary waves (e.g., Sinnett et al. 2018; Davis et al. 2020; Spydell et al. 2021). The leading edge of the waves manifests as a sharp density front where flow convergence occurs (e.g., Shroyer et al. 2009). Studying the evolution and dynamics of these advecting fronts

Corresponding author: X. Wu, x1wu@ucsd.edu

DOI: 10.1175/JTECH-D-21-0072.1

requires techniques for automated coherent front tracking. Previous studies have manually identified the displacement of a single evolving front over a few time steps (e.g., Orton and Jay 2005; Honegger et al. 2017; McSweeney et al. 2020b). Celona et al. (2021) automatically detected a single NLIW front using a Radon transform and tracked the front propagation by computing the two-dimensional cross correlation between each internal solitary wave in the previous and current images. However, this study only tracked a single onshore propagating NLIW front from X-band radar images, and did not consider the existence of multiple fronts or multiple front types, such as wind-driven upwelling fronts and river plume fronts. Up to now no method exists for the automated tracking of a coherently evolving front, especially in coastal ocean environments, where many different types of fronts present simultaneously (Wu et al. 2021b).

In this work, an automated technique is proposed to track coherently evolving density fronts. This technique is applied to the numerical model results presented in Wu et al. (2021b). The realistic model resolved the shelf and surfzone circulation in the San Diego Bight within 50-m water depth and the 3-month study period was characterized by background alongshore density gradient, alongshore pressure driven flows and active internal waves (Wu et al. 2020, 2021c). Density fronts with varied orientation frequently occurred (Wu et al. 2021b). Here the focus is on the alongshore-oriented fronts, as they are more numerous than the cross-shore-oriented fronts and many of these alongshore-oriented fronts persistently move onshore, likely to be onshore propagating NLIW fronts. The manuscript is organized as follows. Configuration of the numerical model is given in section 2. Section 3 describes the front detection and coherent front tracking technique that includes the temporal tracking and a pruning algorithm extracting the coherently evolving frontal segments. Properties of the coherent fronts including the frontal propagation velocity are presented in section 4. Section 5 discusses the optimal selection of several parameters used in the technique and how these may be varied for different scenarios. A summary is provided in section 6.

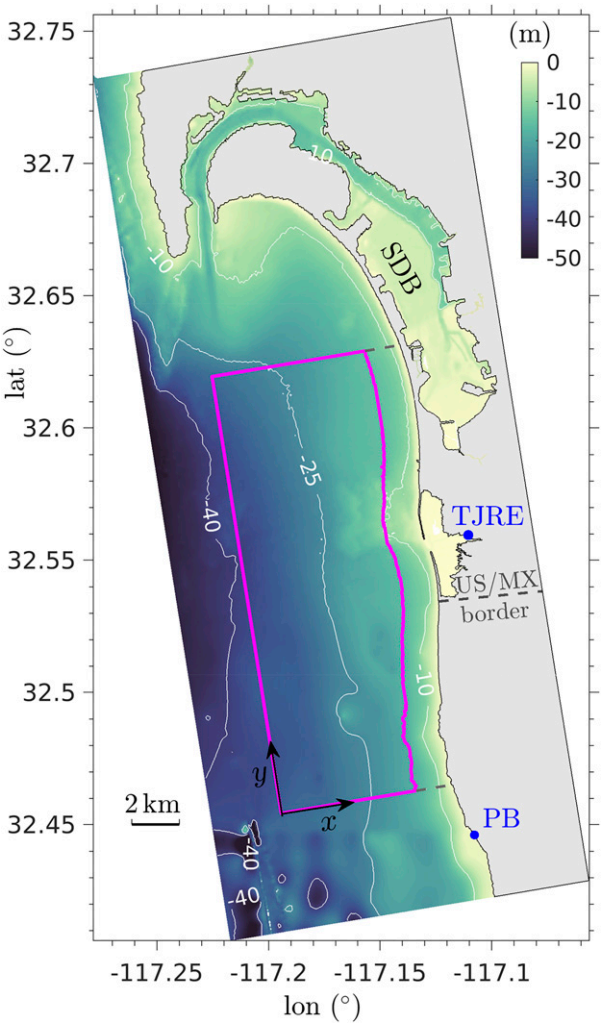

FIG. 1. LV4 grid bathymetry (color shading) and the front study region (magenta line) to which mean front locations are restricted. The (x, y) coordinate system is shown. Blue dots denote the freshwater sources Punta Bandera (PB) and Tijuana River estuary (TJRE). San Diego Bay (SDB) and the U.S.–Mexico border are also labeled.

2. Numerical model configuration

The simulation of the shelf and surfzone circulation uses the Coupled Ocean–Atmosphere–Wave–Sediment Transport (COAWST) model system (Warner et al. 2010; Kumar et al. 2012) that consists of the three-dimensional, hydrostatic Regional Ocean Modeling System (ROMS) circulation model (Shchepetkin and McWilliams 2005) and the Simulating Waves Nearshore model (SWAN) (Booij et al. 1999). Wu et al. (2020) provides a full description of the model configuration. Here only the information essential to this work is provided. The model consists of three one-way nested parent runs (from LV1 to LV2 and then LV3) spanning from the California Current System to the South California Bight, and one downscaled high-resolution child run (LV4) resolving the outer to inner shelf and surfzone in the southern San Diego Bight (Fig. 1). LV4 incorporates surface waves by coupling ROMS with SWAN. NOAA/NAM surface fluxes (wind stress, heat, and precipitation) are applied. Vertical mixing (eddy viscosity and diffusivity) is derived from a k–E submodel (e.g., Umlauf and Burchard 2003). The horizontal eddy viscosity and diffusivity are constant at 0.5 $m^2\ s^{-1}$ over all the model runs. Barotropic tidal elevation and velocities of 10 tidal constituents (M_2, S_2, N_2, K_2, O_1, P_1, Q_1, K_1, M_4, and M_6) are prescribed on the LV1 open boundaries with the amplitudes and phases from the ADCIRC tidal database (Westerink et al. 1993), allowing generation and propagation of internal waves within the model domain (e.g., Kumar et al. 2015; Suanda et al. 2017; Kumar et al. 2019).

The LV4 grid ($15 \times 36\ km^2$, Fig. 1) spans from Punta Bandera (PB), Mexico, to the San Diego Bay (SDB), United States.

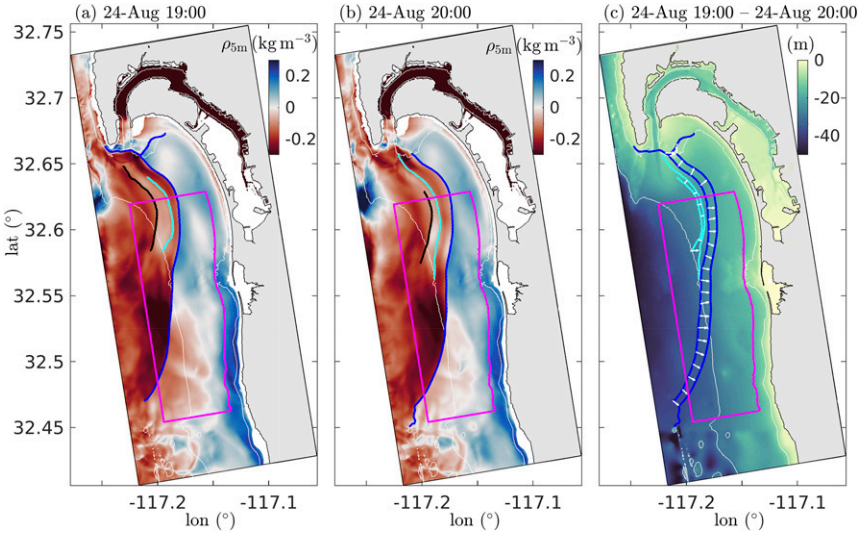

FIG. 2. Density anomaly $\rho_{5\,\mathrm{m}}$ (color shading) at $z = -5$ m and the detected fronts in the model domain at two successive time steps of (a) 1900 and (b) 2000 UTC 24 Aug, and (c) frontal displacements (white arrows) of the two fronts at successive time steps obtained from the front-tracking method. The color shading in (c) represents the bathymetry. The magenta line delineates the front study region.

The horizontal resolution varies from 100 m at the three open boundaries to 8 m near the Tijuana River estuary (TJRE) mouth near the center of the domain. The vertical (z) stretched grid has 15 s-levels with enhanced surface and bottom resolution. The grid receives small and realistic freshwater inputs at PB, TJRE, and small rivers within the SDB. The LV4 run is conducted from July to October 2015 with model outputs saved hourly. Analysis is performed over the summer to fall transition (22 July to 18 October 2015, denoted the *analysis period*). Similar to Wu et al. (2021b), a bounded region (6×18.5 km^2, denoted the *front study region*) is delineated (Fig. 1). The front study region's southern and northern boundaries are 5 km away from the grid's southern open boundary and 7 km from the SDB mouth, respectively. The front study region's western and eastern boundaries are 3 km away from the grid's western open boundary and 1.5 km from the shoreline. An orthogonal coordinate system is defined with an origin at the southeast corner of the front study region (Fig. 1). The cross-shore (x) coordinate is positive onshore and the alongshore (y) is positive northward.

3. Front detection and tracking in time

a. Front detection

Wu et al. (2021b) adopted the Canny edge detection algorithm (Canny 1986) and detected surface density fronts using the surface density from the hourly model outputs. Largely following Wu et al. (2021b), here the density front detection uses the Canny algorithm but applied at a different vertical level. As coherently propagating density fronts, likely induced by shoaling NLIWs, are the focus here, we use the density anomaly (after removing the spatial mean at each time step) at the subsurface level $z = -5$ m ($z = 0$ m at the mean sea surface level), $\rho_{5\mathrm{m}}$, different from the surface density used in Wu et al. (2021b). Similar to Wu et al. (2021b), $\rho_{5\,\mathrm{m}}$ is interpolated onto an equally spaced horizontal grid with a resolution of $\Delta = 40$ m and smoothed using a 2D Gaussian filter with a filter width $\sqrt{2}\Delta$. Then the horizontal density gradient $|\nabla_H \rho|$ is computed by convolving the smoothed density with the spatial derivative of the 2D Gaussian filter (Canny 1986). The algorithm then finds grid points with $|\nabla_H \rho|$ larger than a threshold $|\nabla_H \rho|_c$ and labels them as a *front*. To reduce multiple patchy fronts, the algorithm also tracks the grid points that are connected to the front with a $|\nabla_H \rho|$ larger than a smaller threshold $c|\nabla_H \rho|_c$ ($c = 0.4$ following Wu et al. 2021b), adding these grid points to the front. All connected points are labeled as an individual front.

In the front detection, we apply two additional criteria. First, we require that the total number of front grid points $M \geq 150$, equivalent to a frontal length (estimated as M times grid resolution Δ) ≥ 6 km. This is our choice and in other regions a different length cutoff may be applied. Second, we require that the fronts have a mean front location (i.e., center of mass of the front) located within the front study region (Fig. 1) to minimize the influences from open boundaries, SDB outflows and surf-zone processes, again a choice for this particular configuration. Example fronts that satisfy these criteria are shown on 1900 UTC 24 August (Fig. 2a). The density anomaly $\rho_{5\mathrm{m}}$ is patchy with relatively light water offshore and a cross-shore density difference ~0.3 kg m^{-3} (Fig. 2a). Within the front study region, three density fronts are detected and in the onshore direction the length reaches 7.7 km ($M = 192$, black), 6.8 km ($M = 169$, cyan), and 29.3 km ($M = 733$, blue), respectively. The longest front (blue) separates the offshore lighter water from the onshore denser water and is bifurcated at the northern end.

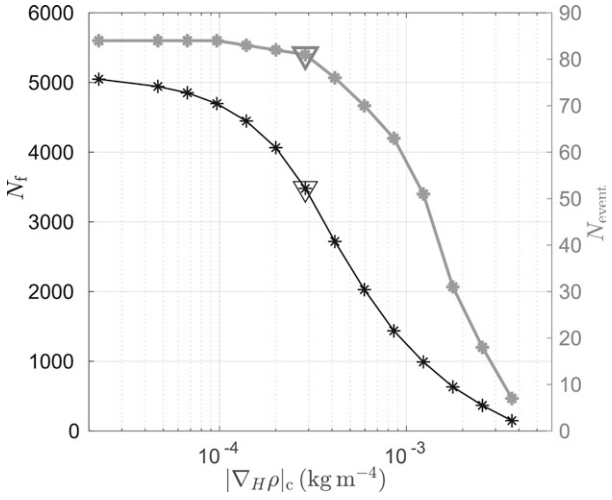

FIG. 3. Total number of the individual fronts N_f (black) and the coherent frontal events N_{event} (gray) vs the cutoff density gradient $|\nabla_H\rho|_c$ using the density anomaly ρ_{5m} at $z = -5$ m. The triangle highlights the value of $|\nabla_H\rho|_c = 2.9 \times 10^{-4}$ kg m^{-4} near the inflection point of the N_f curve. The front events are required to have a duration ≥ 7 h. The N_f and N_{event} values are also listed in Table 1.

Applying the above criteria, the total number N_f of the individual fronts detected during the analysis period is determined by the threshold $|\nabla_H\rho|_c$. The total number decreases from $N_f = 5047$ to 148 as $|\nabla_H\rho|_c$ increases from 0.2×10^{-4} to 36.7×10^{-4} kg m^{-4} (Fig. 3, black). Here the $|\nabla_H\rho|_c$ close to the inflection of the N_f curve (triangle in Fig. 3, $|\nabla_H\rho|_c = 2.9 \times 10^{-4}$ kg m^{-4}) is selected. Using this value, multiple fronts can be detected at one time step. The hourly front number ranges from 0 to 8, and the total number of fronts identified over our analysis period reaches $N_f = 3480$. These $N_f = 3480$ fronts are used for the following analyses. Note that, the same $|\nabla_H\rho|_c$ value was used in Wu et al. (2021b) that focused on cross-shore-oriented surface density fronts, but its sensitivity is discussed in section 5a.

b. Front tracking in time

Following front detection, we develop an algorithm to automatically track coherently propagating fronts in time. At the ith time step for each detected front, the method compares it against each front detected at the $(i + 1)$ time step to identify whether the front coherently propagates. At the ith time step, the jth front $F^{(i,\,j)}$ represents a set of the grid points:

$$F^{(i,\,j)} = \left\{(x_m, y_m)^{(i,\,j)} \middle| m \in \left[1, M^{(i,\,j)}\right]\right\}, \tag{1}$$

where m is the grid point index, (x_m, y_m) is the grid point location, and $M^{(i,\,j)}$ is the total number of the grid points on front $F^{(i,\,j)}$. Similarly, at the $(i + 1)$ time step the kth front $F^{(i+1,\,k)}$ is

$$F^{(i+1,k)} = \left\{(x_l, y_l)^{(i+1,\,k)} \middle| l \in \left[1, M^{(i+1,\,k)}\right]\right\}, \tag{2}$$

where l is the grid point index and $M^{(i+1,\,k)}$ is the total number of the grid points on front $F^{(i+1,\,k)}$. For the mth grid point on front $F^{(i,j)}$, its distance to each grid point on front $F^{(i+1,\,k)}$ is calculated, for instance, the distance to the lth grid point on front $F^{(i+1,\,k)}$ is calculated as

$$s_{(m,l)} = \mathrm{dist}\left((x_m, y_m)^{(i,\,j)}, (x_l, y_l)^{(i+1,\,k)}\right), \tag{3}$$

where dist(·) denotes the 2D Euclidean distance between the two grid points and $s_{(m,\,l)} \geq 0$. The shortest distance $\min(s)_m$ from the grid point $(x_m, y_m)^{(i,\,j)}$ to front $F^{(i+1,\,k)}$ is then calculated as

$$\min(s)_m = \min\left(\left\{s_{(m,\,l)} \middle| l \in \left[1, M^{(i+1,\,k)}\right]\right\}\right), \tag{4}$$

where min(·) denotes the minimum value and this grid point on front $F^{(i+1,\,k)}$ is saved for later usage. The shortest distance to front $F^{(i+1,\,k)}$ is calculated for each grid point on front $F^{(i,\,j)}$. Note, the distance minimization does not give direction of frontal displacements.

Here we focus on the coherently onshore-propagating density fronts. To exclude static density fronts, we require that the shortest distance $\min(s)_m$ is above a lower cutoff s_-. To limit potential front propagation distance within a single time step, an upper limit s_+ is also applied. Grid point $(x_m, y_m)^{(i,j)}$ on front $F^{(i,\,j)}$ is trackable following the shortest distance and matches $(x_l, y_l)^{(i+1,\,k)}$ on front $F^{(i+1,\,k)}$, denoted as $(x_m, y_m)^{(i,\,j)} \rightarrow (x_l, y_l)^{(i+1,\,k)}$, if $s_- \leq \min(s)_m \leq s_+$. In the following, $s_- = 0.2$ km, representing a minimum frontal propagation speed of 5.5 cm s^{-1}. The s_+ should be big enough to cover the range of the hourly frontal displacement, which is dependent on the frontal propagation speed and the background current velocity during the study period. Manual measurement of several hourly frontal displacements yields values approaching 1.2 km. Thus, $s_+ = 1.2$ km is used, allowing a maximum propagation speed of 33.3 cm s^{-1}. Sensitivity testing for (s_-, s_+) is discussed in section 5b. For each grid point on front $F^{(i,\,j)}$, the shortest distance $\min(s)_m$ to front $F^{(i+1,\,k)}$ is calculated and examined against s_- and s_+. Then the total number $\widetilde{M}$ $[\widetilde{M} \leq M^{(i,\,j)}]$ of the trackable grid points on front $F^{(i,\,j)}$ that satisfy $s_- \leq \min(s)_m \leq s_+$ is calculated.

In addition, we calculate the mean cross-shore location $\bar{x}^{(i,\,j)}$ of these $\widetilde{M}$ grid points on front $F^{(i,\,j)}$, together with the mean cross-shore location $\bar{x}^{(i+1,\,k)}$ of the corresponding grid points on front $F^{(i+1,\,k)}$ that are matched to the $\widetilde{M}$ grid points on front $F^{(i,\,j)}$. Using these two mean locations a net cross-shore displacement Δx is estimated:

$$\Delta x = \bar{x}^{(i+1,\,k)} - \bar{x}^{(i,\,j)}. \tag{5}$$

Front $F^{(i+1,\,k)}$ is defined as the forward matched front to front $F^{(i,\,j)}$ if $\Delta x > 0$ (an indication of onshore propagation), $\min(s)_m$ is within the range $[s_-, s_+] = [0.2, 1.2]$ km, and $\widetilde{M} \geq \widetilde{M}_c$, where $\widetilde{M}_c = 150$ is the minimum number of the trackable grid points, corresponding to the 6-km minimum frontal length that we have chosen in the frontal detection procedure (section 3a).

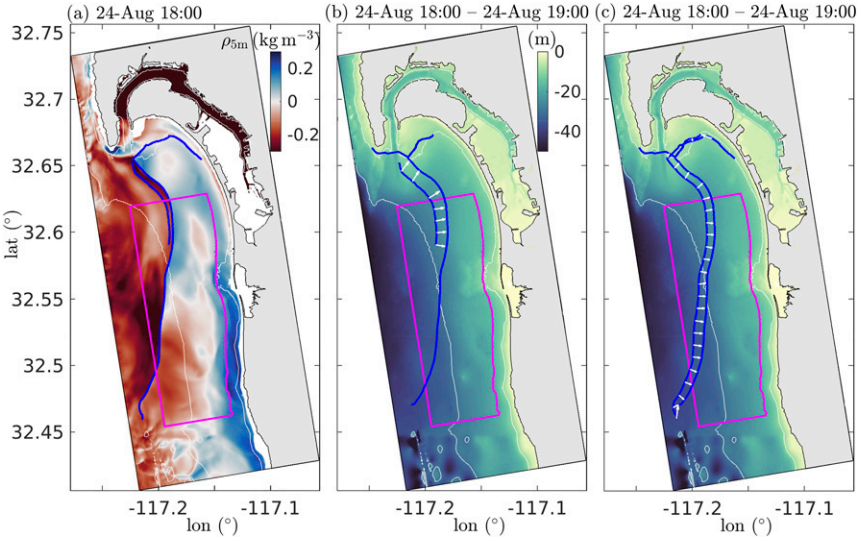

FIG. 4. (a) Example of two fronts detected at 1800 UTC 24 Aug and both fronts can be forward tracked to match the identical front at the next time step (1900 UTC 24 Aug, blue line in Fig. 2a) as shown in (b) and (c). Requiring matching to the longest front (maximum $\widetilde{M}$) keeps the tracking results in (c) and rejects the one in (b).

Front tracking within two successive time steps using the above algorithm is shown in an example (Fig. 2). The density anomaly ρ_{5m} slightly evolves from the first (denoted t_1) to second (denotes t_2) time step. At t_2 three fronts are detected (Fig. 2b). The tracking algorithm examines each front at t_1 and searches for the possible forward matched front at t_2. The longest front (blue) at t_1 has M = 733 grid points (i.e., 29.3 km) and is forward matched with the longest front (blue) at t_2 (Fig. 2c). The matching pair has $\widetilde{M}$ = 606 (i.e., 24.2 km) and the positive Δx indicates an onshore displacement of 620 m. The shortest front (cyan) at t_1 with M = 169 (i.e., 6.8 km) points also has a forward matched front at t_2 (Fig. 2c). The matching pair has $\widetilde{M}$ = 153 (i.e., 6.1 km) and Δx = 300 m. The third (black) front at t_1 is not forward matched to the shortest (black) front at t_2 as $\widetilde{M}$ = 133, less than our cutoff value $\widetilde{M}_c$ = 150. Note that, not all grid points on the front are trackable. For the longest front at t_1, only 4/5 of the grid points show sign of onshore displacement and can be tracked forward. Hereafter, the frontal segment constantly propagating onshore is referred to as an active frontal segment and an example is the frontal segment south of the bifurcation point on the longest front at t_1 (Fig. 2a).

Occasionally, a front [for instance, $F^{(i,\,j)}$] is found to have two or more forward matched fronts at the next (i + 1) time step. In this case, an $\widetilde{M}$ value is obtained for each matching pair and only the forward matched front corresponding to the maximum value of $\widetilde{M}$ (i.e., the longest match) is selected, such that each front only has at most one forward matched front. In addition, there are occasions where two or more fronts at the ith time step are matched to the same front at the (i + 1) time step. Similarly, at the ith time step only the front corresponding to the maximum $\widetilde{M}$ is selected. This situation is shown in an example (Fig. 4). At the first time step (1800 UTC 24 August), two fronts (blue lines in Fig. 4a) are close to each other and they are both matched to the same front (blue line in Fig. 2a) at the next step (1900 UTC 24 August). The matching yields $\widetilde{M}$ = 170 (6.8 km) in Fig. 4b and $\widetilde{M}$ = 604 (24.1 km) in Fig. 4c. The matching pair with a bigger $\widetilde{M}$ (Fig. 4c) is saved in the final results. Overall, the approach guarantees a one-to-one correspondence between two sequential time steps, allowing successive tracking of the same front for multiple time steps.

Applying the above tracking algorithm, an onshore-propagating front can be tracked successively from the hourly model outputs. A collection of the same front moving to different locations is defined as a coherent front event E:

$$E = \left\{F^{(i,\,j)}, F^{(i+1,\,k)}, \ldots, F^{(i+d-1,\,o)}\right\}, \tag{6}$$

where $F^{(i+d-1,o)}$ is the oth front at the (i + d − 1) time step and the tracking ends up at the (i + d − 1) time step. The total number d of time steps contained within event E is defined as the event duration (in hours).

Following the above procedure, coherent front events with varied duration can be identified. Three front event examples with a duration of d = 11, 12, and 13 h are shown in Fig. 5. The first two events contain slightly curved fronts propagating onshore (Figs. 5a,b). During the last 3 h in both events, the front contains an active segment to the south that shows a propagation direction consistent with the previous time steps. To the north the frontal segment deflects from the southern active frontal segment, crossing the front at previous time steps indicating inconsistent front propagation direction. The third event contains a relatively straight front (Fig. 5c) and three of the time steps have been shown in Figs. 2c and 4c. At the fourth and fifth time steps, the front also contains a

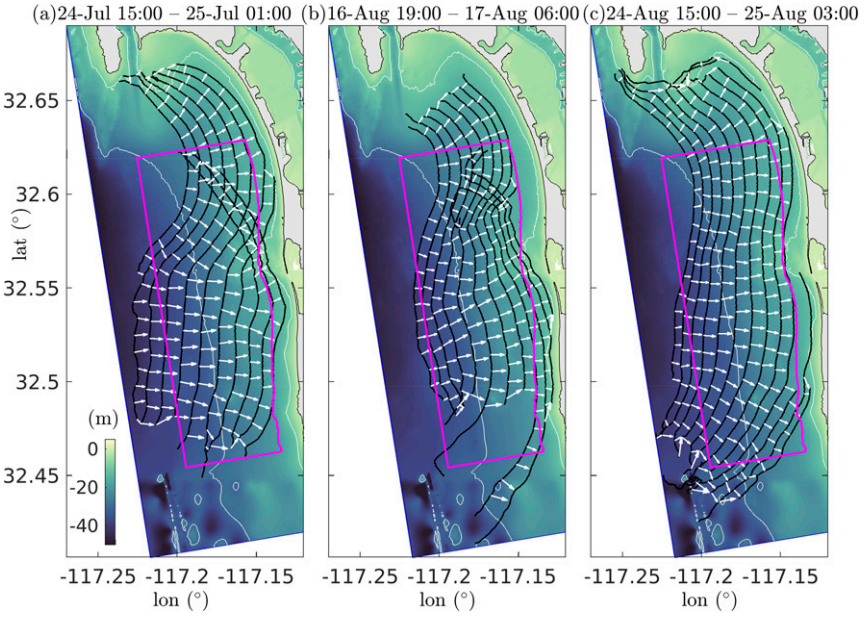

FIG. 5. Example of three coherent front events that have an event duration of (a) d = 11 h (1500 UTC 24 Jul to 0100 UTC 25 Jul), (b) d = 12 h (1900 UTC 16 Aug to 0600 UTC 17 Aug), and (c) d = 13 h (1500 UTC 24 Aug to 0300 UTC 25 Aug) detected using the front-tracking method. These events are the raw results and have not been processed to extract the active frontal segments. The color shading represents the bathymetry.

northern segment that deviates from the southern active segment propagating onshore.

Here, we seek to extract the active frontal segments that have consistent propagation direction. Next, we propose an algorithm to prune the frontal segments with inconsistent propagation direction and extract what we consider the active frontal segments within a front event E.

c. *Extracting active frontal segments*

Here a pruning algorithm is proposed to extract only the active frontal segment (defined here as frontal segments with consistent propagation direction) at each time step within a coherent front event E. Within an event E, a grid point can be tracked successively for multiple time steps as the front moves to new locations, allowing a complete tracking record for each of the grid points. For example, within a front event E [see (6)], a complete tracking record for one grid point initiating from the first time step in E is

$$(x_m, y_m)^{(1)} \rightarrow (x_l, y_l)^{(2)} \rightarrow \cdots \rightarrow (x_q, y_q)^{(n)}, \tag{7}$$

where the superscript denotes the time step within the event E, $(x_m, y_m)^{(1)}$ and $(x_l, y_l)^{(2)}$ are the grid point locations at the first two time steps of the tracking record, $(x_q, y_q)^{(n)}$ is the final location of the tracking record, and $n(1 \leq n \leq d)$ is the total number of time steps contained in the record. Here three complete tracking records are shown in a front event schematic with a duration of d = 4 hours (Fig. 6). The brown point cannot be tracked forward; thus, the record only contains this one point (i.e., n = 1). The four cyan points form a complete record (n = 4) and the three green points (n = 3) form another complete record. Note, a record does not necessarily initiate from the first time step within an event E (e.g., green points in Fig. 6) and does not necessarily terminate at

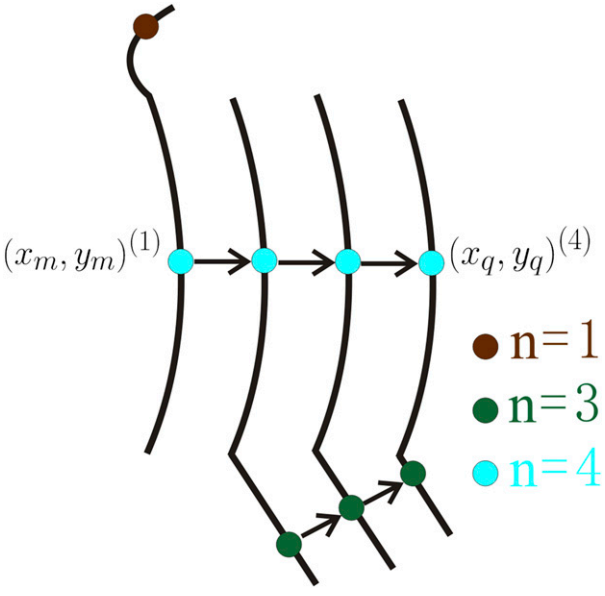

FIG. 6. Schematic of a coherent front event with a duration of d = 4 h and the selected grid points that have three different connectivity n values.

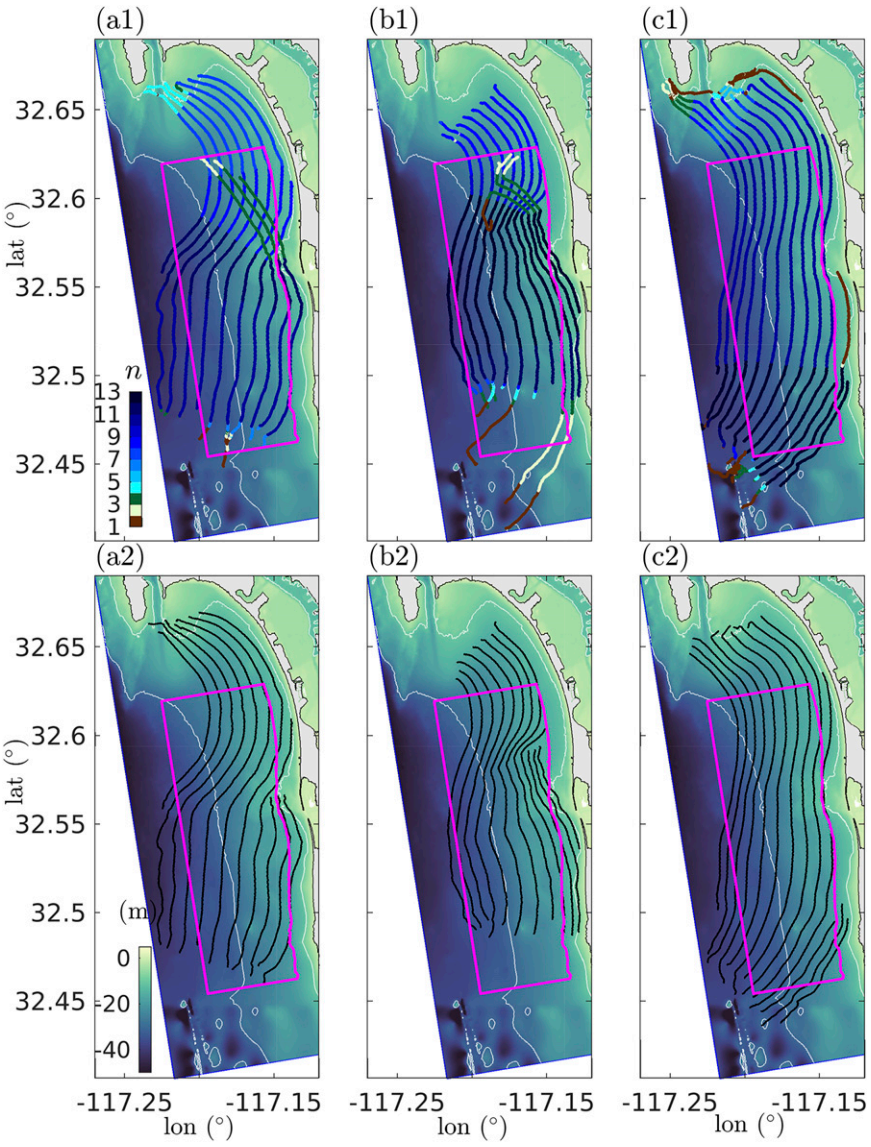

FIG. 7. The connectivity n along the front at each time step during (a1)–(c1) the three front events and (a2)–(c2) the front events after pruning the frontal segments that have $n \leq 3$. The same three front events are shown in Figs. 5a–c. The color shading represents the bathymetry.

the last time step with an event (e.g., brown point in Fig. 6); thus, n can be $\leq d$.

Following construction of the complete record, the tracking record length n is defined as the connectivity of each grid point contained in the record. In the schematic (Fig. 6), the brown point has $n = 1$, and each of the cyan (green) points has $n = 4$ ($n = 3$). The n values within the three front events shown in Fig. 5 are also calculated (Figs. 7a1,b1,c1). The value of n reaches a maximum of 11, 12, and 13, respectively. For the first event (Fig. 7a1), during the last 3 h the northern frontal segment that deflects from the southern segment has $n = 2$ and 3. During the last three hours within the second event, the northern frontal segment also shows low values, $n = 1$, 2, and 3 (Fig. 7b1). At the fourth and fifth hours within the third event (Fig. 7c1), the northern frontal segments have low n values ($n \leq 3$).

Using the connectivity n value, the pruning algorithm then isolates the front at each time step into frontal segments that have $n > n_c$, where n_c is a connectivity cutoff. Within the isolated segments the longest and continuous one is selected as the active frontal segment. In the fronts that we are examining, we found that frontal segments with $n \leq 3$ can deflect from the active frontal segments and show inconsistent propagation direction (examples in Figs. 7a1,b1); thus, $n_c = 3$ is selected here. This cutoff n_c is applied to the three front events (Figs. 7a2,b2,c2). All the frontal segments with $n \leq 3$

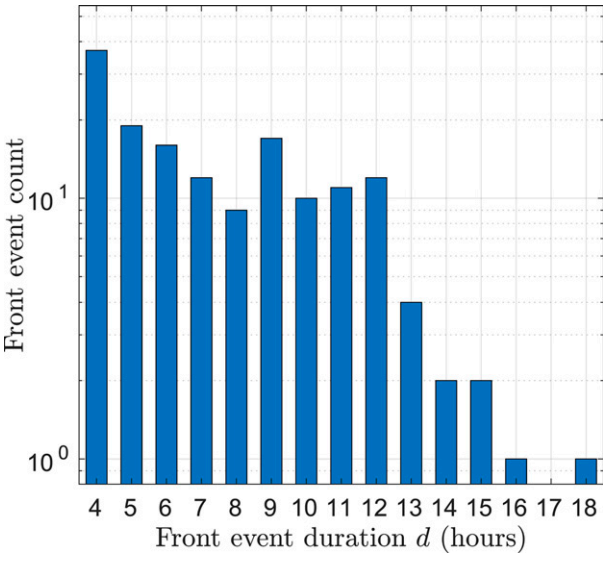

FIG. 8. Histogram of the front event duration d during the 3-month study period.

have been removed and the final results show an active front propagating onshore in each front event. Note that, sometimes the pruning method also removes frontal segments that show consistent propagation direction (see the southern frontal segment at the ninth and tenth time steps in Fig. 7b1 as an example), a compromise to fully remove the segments with inconsistent propagation direction, but which may remove cases such as strong NLIW refraction.

4. Front event properties

Our method for tracking coherently evolving fronts in a front event allows for analyses of evolving fronts. For example, front event properties such as duration, frontal length, frontal orientation, and density gradient can be studied as with individual fronts (e.g., Suanda et al. 2014; Badiey et al. 2016; Wu et al. 2021b). These front event properties could be linked to large-scale processes such as wind-driven upwelling (e.g., Castelao et al. 2006; Kahru et al. 2012), water mass interactions (e.g., Oram et al. 2008), or seasonal variability (e.g., Mauzole et al. 2020). Using the frontal location the frontal propagation velocity can be derived within the 2D area that the front passed by (e.g., Celona et al. 2021). In addition, front evolution during an event can be studied in a Lagrangian approach. Ensemble analysis of multiple front events can also be conducted, similar to the ensemble analysis of multiple individual fronts in Wu et al. (2021b). Here we show examples of front event properties readily calculated using outputs from our tracking method which have a variety of scientific applications.

During the analysis period, the maximum front event duration reaches d = 18 h (Fig. 8), possibly limited by the cross-shore extent (6 km) of the front study region (Fig. 1). Overall, the front event number decreases as the duration increases from d = 4 to 18 h. In total, 72 front events have a duration within 4–6 h, 71 front events have a duration within 7–12 h (two examples in Figs. 5a,b), and 10 events have a duration longer than 12 h (one example in Fig. 5c). Given the hourly displacement upper cutoff s_+ = 1.2 km, the cross-shore extent (6 km) of the front study region allows a minimum event duration of d = 6 h. In the following, we focus on the 81 front events that have a duration $d \geq 7$ h. The total number of individual fronts contained in these events is $N_f^{(\text{event})} = 818$, 24% of the total $N_f = 3480$ fronts (Fig. 3).

Another front event property is the timing when it occurs. Within the 3-month study period, these 81 events span 53 days, resulting in an occurrence frequency of 1.5 events per day (Fig. 9). Front events are not detected from 7 to 20 September, and from 4 October to the model ending time (18 October). We further divide these events into three groups with durations of 7–9, 10–12, and ≥13 h (Fig. 9). Within each group, front events show no sign of concentration within a particular week or month. Knowing front event timing allows for studying processes that are conducive to the generation of front events. For instance, enhanced shelf stratification (e.g., Walter et al. 2014) or shoaling of remotely generated internal tides (Zhang et al. 2015) may promote the generation of NLIW fronts.

Within a front event, frontal propagation speed can be estimated. We define the time elapsed from the beginning of the event as the frontal arrival time t_0. In the example event

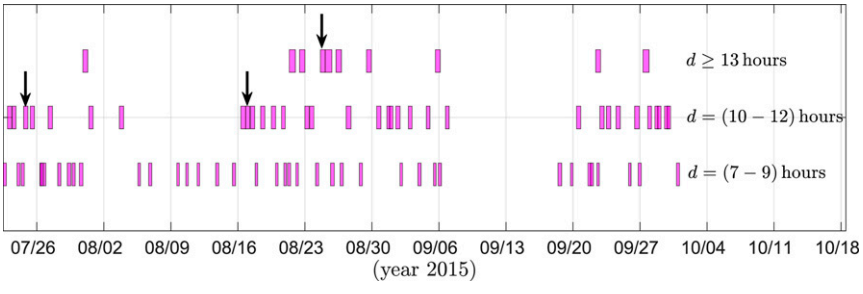

FIG. 9. Time span of the 81 front events that have a duration $d \geq 7$ h. Each event is represented by a magenta box with width representing the event duration. These events are divided into three groups based on the duration. Black arrows denote the three events shown in Figs. 5 and 7.

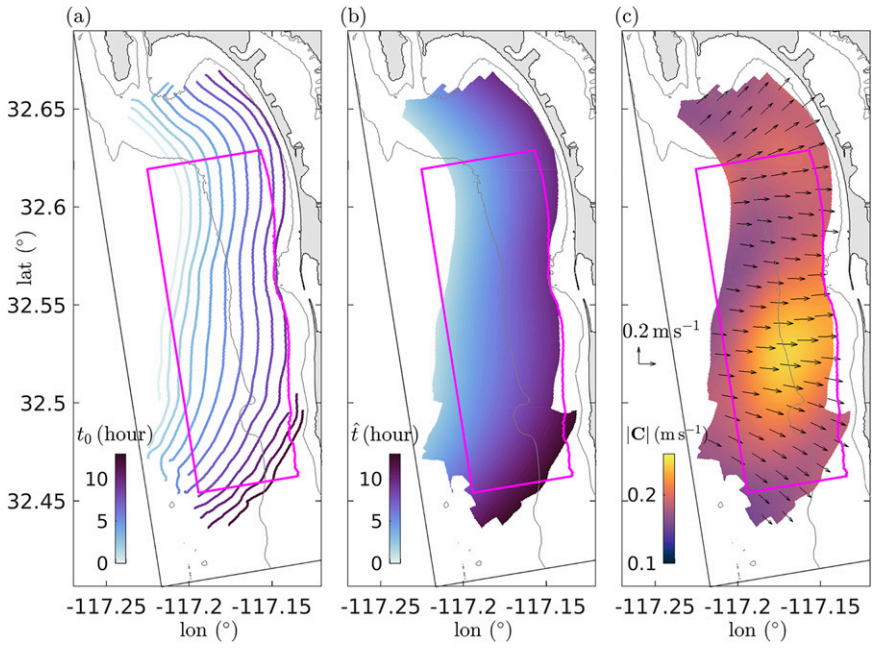

FIG. 10. (a) An example front event colored by the frontal arrival time t_0 in hours, (b) the continuous map of the mapped frontal arrival time $\hat{t}$, and (c) the propagation velocity **C** (vectors) and the propagation speed map (color shading). The same front event is shown in Figs. 5c and 7c2.

shown in Fig. 7c2, t_0 ranges from 0 to 12 h (Fig. 10a). Following Spydell et al. (2021), the arrival times t_0 within the event is smoothly mapped $[\hat{t}(x,y)]$ to the equally spaced horizontal grid and within the 2D area that the front passed by using a smoothing spline interpolation. The interpolation minimizes the cost function Ψ:

TABLE 1. Total number of the individual fronts N_f, front events N_{event} (with a duration $d \geq 7$ h) and fronts contained within all the events $N_f^{(\text{event})}$ under different scenarios with varied filter width, upper density gradient cutoff $|\nabla_H \rho|_c$, ratio c, frontal displacement cutoffs (s_-, s_+), and the minimum number of the trackable grid points $\widetilde{M}_c$.

Scenario	Filter width	$\lvert\nabla_H\rho\rvert_c$ ($\times 10^{-4}$ kg m^{-4})	c	s_- (km)	s_+ (km)	$\widetilde{M}_c$ (length)	N_f	N_{event}	$N_f^{(\text{event})}$
S0	$\sqrt{2}\Delta$	2.9	0.4	0.2	1.2	150 (6 km)	3480	81	818
S1	$\sqrt{4}\Delta$	2.9	0.4	0.2	1.2	150 (6 km)	3401	79	753
S2	$\sqrt{8}\Delta$	2.9	0.4	0.2	1.2	150 (6 km)	3268	79	750
S3	$\sqrt{16}\Delta$	2.9	0.4	0.2	1.2	150 (6 km)	3052	67	633
S4	$\sqrt{32}\Delta$	2.9	0.4	0.2	1.2	150 (6 km)	2604	59	553
S5	$\sqrt{2}\Delta$	0.2	0.4	0.2	1.2	150 (6 km)	5047	84	843
S6	$\sqrt{2}\Delta$	0.4	0.4	0.2	1.2	150 (6 km)	4943	84	843
S7	$\sqrt{2}\Delta$	0.7	0.4	0.2	1.2	150 (6 km)	4852	84	843
S8	$\sqrt{2}\Delta$	1.0	0.4	0.2	1.2	150 (6 km)	4697	84	843
S9	$\sqrt{2}\Delta$	1.4	0.4	0.2	1.2	150 (6 km)	4447	88	834
S10	$\sqrt{2}\Delta$	2.0	0.4	0.2	1.2	150 (6 km)	4065	82	824
S11	$\sqrt{2}\Delta$	4.1	0.4	0.2	1.2	150 (6 km)	2719	76	763
S12	$\sqrt{2}\Delta$	6.0	0.4	0.2	1.2	150 (6 km)	2028	70	689
S13	$\sqrt{2}\Delta$	8.6	0.4	0.2	1.2	150 (6 km)	1437	63	598
S14	$\sqrt{2}\Delta$	12.3	0.4	0.2	1.2	150 (6 km)	991	51	457
S15	$\sqrt{2}\Delta$	17.7	0.4	0.2	1.2	150 (6 km)	632	31	276
S16	$\sqrt{2}\Delta$	25.5	0.4	0.2	1.2	150 (6 km)	367	18	156
S17	$\sqrt{2}\Delta$	36.7	0.4	0.2	1.2	150 (6 km)	148	7	55
S18	$\sqrt{2}\Delta$	2.9	0.1	0.2	1.2	150 (6 km)	4189	83	836
S19	$\sqrt{2}\Delta$	2.9	0.01	0.2	1.2	150 (6 km)	4210	83	836
S20	$\sqrt{2}\Delta$	2.9	0.4	0	1.4	150 (6 km)	3480	88	861
S21	$\sqrt{2}\Delta$	2.9	0.4	0.2	1.2	175 (7 km)	3480	69	677
S22	$\sqrt{2}\Delta$	2.9	0.4	0.2	1.2	200 (8 km)	3480	59	559
S23	$\sqrt{2}\Delta$	2.9	0.4	0.2	1.2	225 (9 km)	3480	47	442

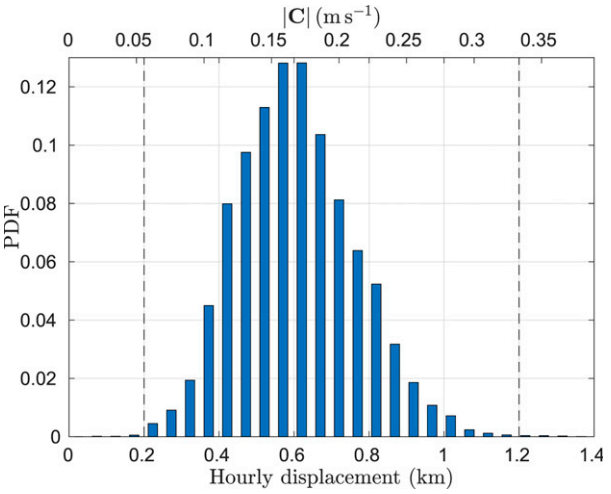

FIG. 11. Probability density function (pdf) of the hourly frontal displacement and the equivalent frontal propagation speed $|\mathbf{C}|$ among all the front events. The front-tracking algorithm uses $(s_-, s_+) = (0, 1.4)$ km.

$$\Psi = \frac{1}{G}\sum_{g=1}^{g=G}\left[t_0(x_g,y_g) - \hat{t}(x_g,y_g)\right]^2 + \lambda^2\frac{A}{2}\int\int\left[\left(\frac{\partial^2\hat{t}}{\partial x^2}\right)^2 + \left(\frac{\partial^2\hat{t}}{\partial y^2}\right)^2\right]dx\,dy, \tag{8}$$

where the sum is over all grid points over all the fronts in the event, $G = M^{(i,j)} + M^{(i+1,k)} + \cdots + M^{(i+d-1,o)}$, $t_0(x_g, y_g)$ is the front arrival time t_0 at the gth grid point, A is the total 2D area that the front passed through, and λ is a constant smoothing parameter. The first term on the rhs is a measure of goodness of fit of t_0, and the second term controls the smoothness where $\lambda = 0.01$ corresponds to length scale of 1.0 km. Figure 10b shows the mapped arrival time $\hat{t}(x,y)$ within the area A that the front passed through. Knowing the mapped arrival time $\hat{t}(x,y)$, the direction and magnitude of the frontal propagation velocity $\mathbf{C}$ can be derived. The direction θ is given by

$$\theta = \tan^{-1}\left(\frac{\partial\hat{t}/\partial y}{\partial\hat{t}/\partial x}\right) \tag{9}$$

and the propagation speed is

$$|\mathbf{C}| = 1\Big/\sqrt{\left(\frac{\partial\hat{t}}{\partial x}\right)^2 + \left(\frac{\partial\hat{t}}{\partial y}\right)^2}. \tag{10}$$

Within the example front event (Fig. 10c), the propagation velocity is not spatially uniform. In the alongshore and northward direction, the propagation direction changes gradually from southeastward to northeastward, suggesting refraction in shallow waters. Meanwhile, the propagation speed reaches a maxima of 0.24 m s^{-1} near 32.52° and the magnitude decreases to both the south and north. Knowing the spatial distribution of $\mathbf{C}$ allows for diagnosing the processes responsible for the front propagation variability in the cross-shore and alongshore directions. Overall, applying the front tracking method enables systematic analyses of front evolution and front event properties.

5. Discussion

Although we have shown results for a particular numerical simulation configuration and a particular type of onshore propagating front, this method can be generalized to be applicable over a wide range of circumstances and front types, such as wind-driven upwelling fronts and river plume fronts. Several frontal detection and tracking parameters are used in our approach which may need to be varied for other circumstances and frontal types. Here, we aim to provide context for making these choices in other situations. We first present sensitivity tests for front detection parameters including filter width, the upper ($|\nabla_H\rho|_c$) and lower ($c|\nabla_H\rho|_c$) density cutoffs, then do the same for front tracking parameters including the frontal displacement cutoffs (s_-, s_+) and the minimum number of the trackable grid points $\widetilde{M}_c$. We also discuss extra steps that can be added to or modified in this method to adapt it to other front scenarios and types.

a. Sensitivity tests for front detection parameters

The front detection method described in section 3a uses a Gaussian filter with a width of $\sqrt{2}\Delta$ (scenario S0 in Table 1) to calculate the density gradient. An increase in the filter width increases the number of neighboring grid points used to calculate the density gradient (Canny 1986), resulting in smoother and broader gradients (Oram et al. 2008). Here sensitivity of the front detection and tracking results to the filter width is examined comparing filter widths of $\sqrt{4}\Delta$, $\sqrt{8}\Delta$, $\sqrt{16}\Delta$, and $\sqrt{32}\Delta$ (scenario S1, S2, S3, and S4, respectively, in Table 1). Under each scenario, we repeat the above procedures using the same front detection and tracking parameters. As in Fig. 9, we consider front events with a duration ≥ 7 h. As the filter width increases from S0 to S4, the total number of the detected fronts N_f decreases from 3480 to 2604, the total event number N_{event} decreases from 81 to 59, and the number $N_f^{(\text{event})}$ of the fronts within the events also monotonically decreases (Table 1). Overall, a smaller filter width ($\sqrt{2}\Delta$) results in the most front events. As pointed out in Oram et al. (2008), the filter width is proportional to the desired front scale normalized by the grid (or image) resolution. In this work the onshore propagating fronts, likely induced by NLIWs, have relatively sharp density gradients and thus a small filter width is preferred. Other studies of fronts with a relatively broad gradient may require a larger filter width.

Sensitivity of the front tracking results to the upper ($|\nabla_H\rho|_c$) and lower($c|\nabla_H\rho|_c$) density gradient cutoffs is also examined. First, we only change $|\nabla_H\rho|_c$ and keep other parameters unchanged. As $|\nabla_H\rho|_c$ increases from 0.2×10^{-4} to 36.7×10^{-4} kg m^{-4} (S5 to S17 in Table 1), the total front event number N_{event} decreases from 84 to 7 (Fig. 3, gray). At the selected value of $|\nabla_H\rho|_c = 2.9 \times 10^{-4}$ kg m^{-4}, N_{event} starts to reach a plateau. A smaller $|\nabla_H\rho|_c$ results in more individual

density fronts, whereas N_{event} only slightly increases by 1–3 (Fig. 3). Second, we only change c (the lower cutoff) and maintain the other parameters. Previous studies have used different c values, from 0.4 (Castelao et al. 2006) to 0.1 (Kurekin et al. 2020). A smaller c is expected to result in more density fronts. Here, as c decreases from 0.4 to 0.1 and further to 0.01 (scenario S0, S18, and S19, respectively), the total number of fronts N_f increases by 20% in S18 and S19 (compared with S0, Table 1), whereas N_{event} only increases by 2 and $N_f^{(event)}$ slightly increases. Overall, a smaller $|\nabla_H\rho|_c$ or c only adds 2–3 additional front events, likely because an increase in detected fronts is not coherently trackable. These results are also potentially due to the kinematics of the targeted fronts, which have relatively sharp and strong density gradients. In other front studies, the choice of $|\nabla_H\rho|_c$ and c depends on the density gradient magnitude of the targeted fronts and potentially frontal kinematics. For instance, the density gradient reaches $O(10^{-3})$ kg m^{-4} over a few hundred meters for a river plume front (e.g., Lentz et al. 2003).

b. Sensitivity tests for front tracking parameters

In the front tracking steps (section 3b), the hourly frontal displacement is required to be within the range $[s_-, s_+] = [0.2, 1.2]$ km. The rationale of selecting these two cutoff values is examined here. We repeat the above front tracking procedures using the same $\widetilde{M}_c$. The only change is applying a wider range $[s_-, s_+] = [0, 1.4]$ km (S20 in Table 1). The tracking identifies $N_{event} = 88$ front events (with a duration ≥ 7 h) that contain $N_f^{(event)} = 861$ individual fronts. Thus, using the wider range only 7 more front events are detected. In addition, for each of the 88 front events, we extract the active frontal segments using the pruning algorithm and then calculate the 2D map of the frontal propagation velocity **C**. From the 2D map results, the probability density function (pdf) of the velocity magnitude $|\mathbf{C}|$, and the equivalent hourly displacement over all these events can be quantified (Fig. 11). The pdf shows a unimodal distribution with a peak around $|\mathbf{C}| = 0.17$ m s^{-1}, equivalent to a hourly displacement of 0.6 km (Fig. 11). The hourly displacement concentrates within 0.4–0.8 km and the cumulative probability within this range reaches 80%. Approaching the lower ($s_- = 0.2$ km) or upper ($s_+ = 1.2$ km) bound in S0, the pdf value becomes negligible, supporting that the two cutoff values in S0 are suitable to track the coherent front events here. Note that, the modeled front propagation speed is similar to the observed internal bore propagation speed (i.e., 0.1–0.3 m s^{-1}) off the central California coast (e.g., McSweeney et al. 2020b; Spydell et al. 2021). Other situations may require adjustment of temporal displacement cutoff values. For example, previous studies have shown that NLIWs can propagate with a speed ~0.8 m s^{-1} on a continental shelf (Shroyer et al. 2011), and up to 3 m s^{-1} in the South China Sea (Alford et al. 2010). River plume fronts propagating at ~0.5 m s^{-1} were also reported (Lentz et al. 2003). In these regions, applying this front tracking method would require adjustment of (s_-, s_+).

In addition, sensitivity of the tracking results to the minimum number of the trackable grid points $\widetilde{M}_c$ is also examined. Here we use the same $(s_-, s_+) = (0.2, 1.2)$ km but alter $\widetilde{M}_c$ from 150 (equivalent to 6 km, S0) to 175 (7 km, S21), 200 (8 km, S22), and 225 (9 km, S23). The 6 km frontal length cutoff in our front detection steps (section 3a) does not allow a test for $\widetilde{M}_c < 150$. As $\widetilde{M}_c$ increases from 150, the total frontal event number N_{event} decreases by 15% (S21), 27% (S22), and 42% (S23) (Table 1). Thus, the total number of front events is more sensitive to $\widetilde{M}_c$ than the front detection parameters ($|\nabla_H\rho|_c$ and c). Given that frontal length can be affected by interactions between the front and other physical processes, a strong front (strong density gradient) is not necessarily a long front. Thus, in other front studies, tuning may be needed to seek an appropriate $\widetilde{M}_c$ value that matches the fronts of interest. Overall, applying (s_-, s_+) and $\widetilde{M}_c$ successfully tracks coherently evolving fronts when multiple fronts are present simultaneously. This situation is challenging for the only other automated front tracking approach that has been applied to X-band radar observations to track a single propagating front (Celona et al. 2021). Moreover, by applying (s_-, s_+) the present tracking method easily calculates the connectivity n and removes the frontal segments showing inconsistent propagation direction (section 3c).

c. Adjustments to generalize the method

Extra steps can be added to generalize the present front tracking method. Here we briefly describe two extra steps. The front tracking steps (section 3b) require a net positive (onshore) cross-shore displacement defined in (5) to narrow down the searching for the forward matched front $F^{(i+1,k)}$. In other cases, like wind-driven upwelling fronts (e.g., Austin and Barth 2002) and river plume fronts (e.g., Honegger et al. 2017), frontal displacement is not necessarily unidirectional (e.g., oscillated by barotropic tides). In such cases, the criterion using (5) can be neglected, or replaced by another criterion to narrow down the search range. For instance, an alternative criterion could be to require the horizontal density gradient vectors of front $F^{(i,j)}$ and $F^{(i+1,k)}$ to have similar magnitudes and directions as used in front detection by Cayula and Cornillon (1995).

If there are two or more front matching pairs, the front tracking steps (section 3b) select the maximum $\widetilde{M}$ achieving a one-to-one correspondence between two sequential time steps. Occasionally, a coherently propagating front can become discontinuous and break into two or more shorter segments at a certain time step, resulting in multiple front matching pairs. In this case, these shorter front segments can be joined into one single continuous front to yield a single front matching pair. An example front joining algorithm is provided in Simonin et al. (2009) that detected fronts from radar images.

6. Summary

Here we present an automated method to temporally track coherently evolving density fronts and apply the method to numerical model solutions. The automated method consists of three components. First, at all time steps individual density

fronts are detected using the Canny edge detection algorithm with a specific filter width, upper ($|\nabla_H\rho|_c$) and lower ($c|\nabla_H\rho|_c$) density gradient cutoffs, and minimum front length. Next, a temporal front tracking algorithm is developed that compares a front at time step i to each front at time step $i + 1$ to determine if the i front is forward matched to the $i + 1$ front. The comparison examines each grid point on the i front and calculates the minimum distance from this grid point to the $i + 1$ front. If the minimum distance falls within a range of $[s_-, s_+]$, this grid point on the i front is considered trackable. If the total number of the trackable grid points on the i front exceeds a cutoff $\widetilde{M}_c$, the i front is considered forward matched to the $i + 1$ front. When the i front is forward matched to multiple fronts at the $i + 1$ time step, or multiple fronts at the i time step are forward matched to an identical front at the $i + 1$ time step, only the front with the largest number of the trackable grid points is saved. This approach allows forward temporal tracking of a front for multiple time steps forming a front event. Last, a pruning algorithm is proposed. Within an event, the total number of time steps that a grid point can be tracked is its connectivity n. A pruning algorithm is applied to a front event to retain only the coherently evolving frontal segments with a connectivity n exceeding a cutoff value n_c. This automated front tracking method is applied to a realistic 3-month San Diego Bight model solution yielding 81 front events with duration ≥ 7 h. This method allows analyses of front event properties, such as event duration, occurrence frequency, and spatial distribution of the frontal propagation velocity. The sensitivity of the front detection (filter width, $|\nabla_H\rho|_c$, and $c|\nabla_H\rho|_c$) and tracking (s_-, s_+, and $\widetilde{M}_c$) parameters is also examined. A smaller filter width is suggested if targeted fronts have a sharp density gradient. In our case, the total number of the front events is more sensitive to the minimum number of the trackable grid points $\widetilde{M}_c$ compared with the density gradient cutoffs ($|\nabla_H\rho|_c$ and $c|\nabla_H\rho|_c$) and the frontal displacement cutoffs (s_-, s_+). In other front studies the selection of $\widetilde{M}_c$ may require tuning. Overall, with straightforward adjustments this automated front tracking method can be applied to temporally track evolving fronts of varying types in other regions, such as wind-driven upwelling fronts, river plume fronts and nonlinear internal wave fronts.

Acknowledgments. This work was supported by the National Science Foundation (OCE-1459389) as part of the Cross-Surfzone/Inner-shelf Dye Exchange (CSIDE) experiment. Additional funding is through the Environmental Protection Agency through the North American Development Bank; however, it does not necessarily reflect the policies, actions, or positions of the U.S. EPA or NADB. This work used the Extreme Science and Engineering Discovery Environment (XSEDE), which is supported by National Science Foundation (ACI-1548562). The numerical simulations were performed on the comet cluster at the San Diego Super Computer Center through XSEDE Allocation TG-OCE180013. NOAA provided the NAM atmospheric forcing fields and the bathymetry. SIO Coastal Data Information Program provided wave forcing. Ganesh Gopalakrishnan and Bruce Cornuelle provided CASE model solutions for outer grid boundary conditions which are available online (http://ecco.ucsd.edu/case.html). We also appreciate extra support from the Tijuana River National Estuarine Research Reserve and the Southern California Coastal Ocean Observing System. Our method is written in MATLAB and the codes are available through Zenodo at https://doi.org/10.5281/zenodo.5540392 (Wu et al. 2021a) or by contacting the corresponding author.

REFERENCES

Acha, E. M., H. W. Mianzan, R. A. Guerrero, M. Favero, and J. Bava, 2004: Marine fronts at the continental shelves of austral South America: Physical and ecological processes. *J. Mar. Syst.*, **44**, 83–105, https://doi.org/10.1016/j.jmarsys.2003.09.005.

Alford, M. H., R.-C. Lien, H. Simmons, J. Klymak, S. Ramp, Y. J. Yang, D. Tang, and M.-H. Chang, 2010: Speed and evolution of nonlinear internal waves transiting the South China Sea. *J. Phys. Oceanogr.*, **40**, 1338–1355, https://doi.org/10.1175/2010JPO4388.1.

Austin, J. A., and J. A. Barth, 2002: Variation in the position of the upwelling front on the Oregon shelf. *J. Geophys. Res.*, **107**, 3180, https://doi.org/10.1029/2001JC000858.

——, and S. J. Lentz, 2002: The inner shelf response to wind-driven upwelling and downwelling. *J. Phys. Oceanogr.*, **32**, 2171–2193, https://doi.org/10.1175/1520-0485(2002)032<2171:TISRTW>2.0.CO;2.

Badiey, M., L. Wan, and J. F. Lynch, 2016: Statistics of nonlinear internal waves during the shallow water 2006 experiment. *J. Atmos. Oceanic Technol.*, **33**, 839–846, https://doi.org/10.1175/JTECH-D-15-0221.1.

Banas, N., P. MacCready, and B. Hickey, 2009: The Columbia River plume as cross-shelf exporter and along-coast barrier. *Cont. Shelf Res.*, **29**, 292–301, https://doi.org/10.1016/j.csr.2008.03.011.

Belkin, I. M., 2021: Remote sensing of ocean fronts in marine ecology and fisheries. *Remote Sens.*, **13**, 883, https://doi.org/10.3390/rs13050883.

Booij, N., R. C. Ris, and L. H. Holthuijsen, 1999: A third-generation wave model for coastal regions: 1. Model description and validation. *J. Geophys. Res.*, **104**, 7649–7666, https://doi.org/10.1029/98JC02622.

Canny, J., 1986: A computational approach to edge detection. *IEEE Trans. Pattern Anal. Mach. Intell.*, **PAMI-8**, 679–698, https://doi.org/10.1109/TPAMI.1986.4767851.

Castelao, R. M., T. P. Mavor, J. A. Barth, and L. C. Breaker, 2006: Sea surface temperature fronts in the California Current System from geostationary satellite observations. *J. Geophys. Res.*, **111**, C09026, https://doi.org/10.1029/2006JC003541.

Cayula, J.-F., and P. Cornillon, 1992: Edge detection algorithm for SST images. *J. Atmos. Oceanic Technol.*, **9**, 67–80, https://doi.org/10.1175/1520-0426(1992)009<0067:EDAFSI>2.0.CO;2.

——, and ——, 1995: Multiple-image edge detection for SST images. *J. Atmos. Oceanic Technol.*, **12**, 821–829, https://doi.org/10.1175/1520-0426(1995)012<0821:MIEDFS>2.0.CO;2.

Celona, S., S. T. Merrifield, T. de Paolo, N. Kaslan, T. Cook, E. J. Terrill, and J. A. Colosi, 2021: Automated detection, classification, and tracking of internal wave signatures using X-band radar in the inner shelf. *J. Atmos. Oceanic Technol.*, **38**, 789–803, https://doi.org/10.1175/JTECH-D-20-0129.1.

Chakraborty, K., S. Maity, A. A. Lotliker, A. Samanta, J. Ghosh, N. Masuluri, N. Swetha, and R. P. Bright, 2019: Modelling of marine ecosystem in regional scale for short term prediction of satellite-aided operational fishery advisories. *J. Oper.*

Oceanogr., **12** (Suppl. 2), S157–S175, https://doi.org/10.1080/1755876X.2019.1574951.

Colosi, J. A., N. Kumar, S. H. Suanda, T. M. Freismuth, and J. H. MacMahan, 2018: Statistics of internal tide bores and internal solitary waves observed on the inner continental shelf off Point Sal, California. *J. Phys. Oceanogr.*, **48**, 123–143, https://doi.org/10.1175/JPO-D-17-0045.1.

Connolly, T. P., and A. R. Kirincich, 2019: High-resolution observations of subsurface fronts and alongshore bottom temperature variability over the inner shelf. *J. Geophys. Res. Oceans*, **124**, 593–614, https://doi.org/10.1029/2018JC014454.

D'Asaro, E., C. Lee, L. Rainville, R. Harcourt, and L. Thomas, 2011: Enhanced turbulence and energy dissipation at ocean fronts. *Science*, **332**, 318–322, https://doi.org/10.1126/science.1201515.

Dauhajre, D. P., J. C. McWilliams, and Y. Uchiyama, 2017: Submesoscale coherent structures on the continental shelf. *J. Phys. Oceanogr.*, **47**, 2949–2976, https://doi.org/10.1175/JPO-D-16-0270.1.

Davis, K. A., R. S. Arthur, E. C. Reid, J. S. Rogers, O. B. Fringer, T. M. DeCarlo, and A. L. Cohen, 2020: Fate of internal waves on a shallow shelf. *J. Geophys. Res. Oceans*, **125**, e2019JC015377, https://doi.org/10.1029/2019JC015377.

Farrar, J. T., C. J. Zappa, R. A. Weller, and A. T. Jessup, 2007: Sea surface temperature signatures of oceanic internal waves in low winds. *J. Geophys. Res.*, **112**, C06014, https://doi.org/10.1029/2006JC003947.

Giddings, S. N., and Coauthors, 2012: Frontogenesis and frontal progression of a trapping-generated estuarine convergence front and its influence on mixing and stratification. *Estuaries Coasts*, **35**, 665–681, https://doi.org/10.1007/s12237-011-9453-z.

Grimes, D. J., F. Feddersen, S. N. Giddings, and G. Pawlak, 2020: Cross-shore deformation of a surfzone-released dye plume by an internal tide on the inner shelf. *J. Phys. Oceanogr.*, **50**, 35–54, https://doi.org/10.1175/JPO-D-19-0046.1.

Hally-Rosendahl, K., F. Feddersen, D. B. Clark, and R. Guza, 2015: Surfzone to inner-shelf exchange estimated from dye tracer balances. *J. Geophys. Res. Oceans*, **120**, 6289–6308, https://doi.org/10.1002/2015JC010844.

Honegger, D. A., M. C. Haller, W. R. Geyer, and G. Farquharson, 2017: Oblique internal hydraulic jumps at a stratified estuary mouth. *J. Phys. Oceanogr.*, **47**, 85–100, https://doi.org/10.1175/JPO-D-15-0234.1.

Hopkins, J., P. Challenor, and A. G. P. Shaw, 2010: A new statistical modeling approach to ocean front detection from SST satellite images. *J. Atmos. Oceanic Technol.*, **27**, 173–191, https://doi.org/10.1175/2009JTECHO684.1.

Horner-Devine, A. R., R. D. Hetland, and D. G. MacDonald, 2015: Mixing and transport in coastal river plumes. *Annu. Rev. Fluid Mech.*, **47**, 569–594, https://doi.org/10.1146/annurev-fluid-010313-141408.

Kahru, M., E. Di Lorenzo, M. Manzano-Sarabia, and B. G. Mitchell, 2012: Spatial and temporal statistics of sea surface temperature and chlorophyll fronts in the California Current. *J. Plankton Res.*, **34**, 749–760. https://doi.org/10.1093/plankt/fbs010.

——, M. G. Jacox, and M. D. Ohman, 2018: CCE1: Decrease in the frequency of oceanic fronts and surface chlorophyll concentration in the California Current System during the 2014–2016 northeast Pacific warm anomalies. *Deep-Sea Res. I*, **140**, 4–13, https://doi.org/10.1016/j.dsr.2018.04.007.

Kumar, N., G. Voulgaris, J. C. Warner, and M. Olabarrieta, 2012: Implementation of the vortex force formalism in the Coupled Ocean-Atmosphere-Wave-Sediment Transport (COAWST) modeling system for inner shelf and surf zone applications. *Ocean Modell.*, **47**, 65–95, https://doi.org/10.1016/j.ocemod.2012.01.003.

——, F. Feddersen, Y. Uchiiyama, J. McWilliams, and W. O. Reilly, 2015: Midshelf to surfzone coupled ROMS-SWAN model data comparison of waves, currents, and temperature: Diagnosis of subtidal forcings and response. *J. Phys. Oceanogr.*, **45**, 1464–1490, https://doi.org/10.1175/JPO-D-14-0151.1.

——, S. H. Suanda, J. A. Colosi, K. Haas, E. Di Lorenzo, A. J. Miller, and C. A. Edwards, 2019: Coastal semidiurnal internal tidal incoherence in the Santa Maria Basin, California: Observations and model simulations. *J. Geophys. Res. Oceans*, **124**, 5158–5179, https://doi.org/10.1029/2018JC014891.

Kurekin, A. A., P. E. Land, and P. I. Miller, 2020: Internal waves at the UK continental shelf: Automatic mapping using the ENVISAT ASAR sensor. *Remote Sens.*, **12**, 2476, https://doi.org/10.3390/rs12152476.

Lentz, S. J., S. Elgar, and R. Guza, 2003: Observations of the flow field near the nose of a buoyant coastal current. *J. Phys. Oceanogr.*, **33**, 933–943, https://doi.org/10.1175/1520-0485(2003)33<933:OOTFFN>2.0.CO;2.

Lévy, M., P. J. Franks, and K. S. Smith, 2018: The role of submesoscale currents in structuring marine ecosystems. *Nat. Commun.*, **9**, 4758, https://doi.org/10.1038/s41467-018-07059-3.

Mauzole, Y., H. Torres, and L.-L. Fu, 2020: Patterns and dynamics of SST fronts in the California Current System. *J. Geophys. Res. Oceans*, **125**, e2019JC015499, https://doi.org/10.1029/2019JC015499.

McSweeney, J. M., and Coauthors, 2020a: Observations of shoaling nonlinear internal bores across the central California inner shelf. *J. Phys. Oceanogr.*, **50**, 111–132, https://doi.org/10.1175/JPO-D-19-0125.1.

——, and Coauthors, 2020b: Alongshore variability of shoaling internal bores on the inner shelf. *J. Phys. Oceanogr.*, **50**, 2965–2981, https://doi.org/10.1175/JPO-D-20-0090.1.

Nagai, T., N. Gruber, H. Frenzel, Z. Lachkar, J. C. McWilliams, and G.-K. Plattner, 2015: Dominant role of eddies and filaments in the offshore transport of carbon and nutrients in the California Current System. *J. Geophys. Res. Oceans*, **120**, 5318–5341, https://doi.org/10.1002/2015JC010889.

Oram, J. J., J. C. McWilliams, and K. D. Stolzenbach, 2008: Gradient-based edge detection and feature classification of sea-surface images of the Southern California Bight. *Remote Sens. Environ.*, **112**, 2397–2415, https://doi.org/10.1016/j.rse.2007.11.010.

Orton, P. M., and D. A. Jay, 2005: Observations at the tidal plume front of a high-volume river outflow. *Geophys. Res. Lett.*, **32**, L11605, https://doi.org/10.1029/2005GL022372.

Pineda, J., 1999: Circulation and larval distribution in internal tidal bore warm fronts. *Limnol. Oceanogr.*, **44**, 1400–1414, https://doi.org/10.4319/lo.1999.44.6.1400.

Shchepetkin, A. F., and J. C. McWilliams, 2005: The Regional Oceanic Modeling System (ROMS): A split-explicit, free-surface, topography-following-coordinate oceanic model. *Ocean Modell.*, **9**, 347–404, https://doi.org/10.1016/j.ocemod.2004.08.002.

Shroyer, E. L., J. N. Moum, and J. D. Nash, 2009: Observations of polarity reversal in shoaling nonlinear internal waves. *J. Phys. Oceanogr.*, **39**, 691–701, https://doi.org/10.1175/2008JPO3953.1.

——, ——, and ——, 2011: Nonlinear internal waves over New Jersey's continental shelf. *J. Geophys. Res.*, **116**, C03022, https://doi.org/10.1029/2010JC006332.

Simonin, D., A. R. Tatnall, and I. S. Robinson, 2009: The automated detection and recognition of internal waves. *Int. J. Remote Sens.*, **30**, 4581–4598, https://doi.org/10.1080/01431160802621218.

Sinnett, G., F. Feddersen, A. J. Lucas, G. Pawlak, and E. Terrill, 2018: Observations of nonlinear internal wave run-up to the surfzone. *J. Phys. Oceanogr.*, **48**, 531–554, https://doi.org/10.1175/JPO-D-17-0210.1.

Spydell, M. P., and Coauthors, 2021: Internal bore evolution across the shelf near Point Sal, California, interpreted as a gravity current. *J. Phys. Oceanogr.*, https://doi.org/10.1175/JPO-D-21-0095.1, in press.

Suanda, S. H., J. A. Barth, R. A. Holman, and J. Stanley, 2014: Shore-based video observations of nonlinear internal waves across the inner shelf. *J. Atmos. Oceanic Technol.*, **31**, 714–728, https://doi.org/10.1175/JTECH-D-13-00098.1.

——, F. Feddersen, and N. Kumar, 2017: The effect of barotropic and baroclinic tides on coastal stratification and mixing. *J. Geophys. Res. Oceans*, **122**, 10 156–10 173, https://doi.org/10.1002/2017JC013379.

Ullman, D. S., and P. C. Cornillon, 2000: Evaluation of front detection methods for satellite-derived SST data using in situ observations. *J. Atmos. Oceanic Technol.*, **17**, 1667–1675, https://doi.org/10.1175/1520-0426(2000)017<1667:EOFDMF>2.0.CO;2.

Umlauf, L., and H. Burchard, 2003: A generic length-scale equation for geophysical turbulence models. *J. Mar. Res.*, **61**, 235–265, https://doi.org/10.1357/002224003322005087.

Walter, R. K., C. B. Woodson, P. R. Leary, and S. G. Monismith, 2014: Connecting wind-driven upwelling and offshore stratification to nearshore internal bores and oxygen variability. *J. Geophys. Res. Oceans*, **119**, 3517–3534, https://doi.org/10.1002/2014JC009998.

Warner, J. C., B. Armstrong, R. He, and J. B. Zambon, 2010: Development of a Coupled Ocean–Atmosphere–Wave–Sediment Transport (COAWST) modeling system. *Ocean Modell.*, **35**, 230–244, https://doi.org/10.1016/j.ocemod.2010.07.010.

Westerink, J., R. Luettich, and N. Scheffner, 1993: ADCIRC: An advanced three-dimensional circulation model for shelves, coasts, and estuaries: Report 3—Development of a tidal constituent database for the western north Atlantic and Gulf of Mexico. Coastal Engineering Research Center Tech. Rep., 150 pp.

Wu, X., F. Feddersen, S. N. Giddings, N. Kumar, and G. Gopalakrishnan, 2020: Mechanisms of mid- to outer-shelf transport of shoreline-released tracers. *J. Phys. Oceanogr.*, **50**, 1813–1837, https://doi.org/10.1175/JPO-D-19-0225.1.

——, ——, and ——, 2021a: Automated temporal front tracking toolbox in MATLAB (1.0). Zenodo, https://doi.org/10.5281/zenodo.5540392.

——, ——, and ——, 2021b: Characteristics and dynamics of density fronts over the inner to midshelf under weak wind conditions. *J. Phys. Oceanogr.*, **51**, 789–808, https://doi.org/10.1175/JPO-D-20-0162.1.

——, ——, and ——, 2021c: Diagnosing surfzone impacts on inner-shelf flow spatial variability using realistic model experiments with and without surface gravity waves. *J. Phys. Oceanogr.*, **51**, 2505–2515, https://doi.org/10.1175/JPO-D-20-0324.1.

Zhang, S., M. H. Alford, and J. B. Mickett, 2015: Characteristics, generation and mass transport of nonlinear internal waves on the Washington continental shelf. *J. Geophys. Res. Oceans*, **120**, 741–758, https://doi.org/10.1002/2014JC010393.